International Journal of Nanomedicine

Dovepress
Taylor & Francis Group

Open Access Full Text Article

ORIGINAL RESEARCH

Dopamine and Mn(II) Chelate Covalent-Doping Coated Ti(IV)-Nanotheranostics for Magnetic Resonance Imaging Guided Phototherapy in Oral Cancer

Zhenghui Li[1–3,*], Xufei Bian[1,*], Huiyu Wu[1], Ling He[1], Zuhua Zeng[1], Lei Zhong[1], Yao Liu[1], Yu Li[1], Guihao Hu[1], Fanglin Mi[2], Zhen Liu[2], Jiang Zhu[1]

[1]Medical Imaging Key Laboratory of Sichuan Province, North Sichuan Medical College, Nanchong, Sichuan, People's Republic of China; [2]Department of Stomatology, Affiliated Hospital of North Sichuan Medical College, Nanchong, Sichuan, People's Republic of China; [3]Beijing Anzhen Nanchong Hospital, Capital Medical University & Nanchong Central Hospital, Nanchong, Sichuan, People's Republic of China

*These authors contributed equally to this work

Correspondence: Zhen Liu, Department of Stomatology, Affiliated Hospital of North Sichuan Medical College, Nanchong, Sichuan, 637100, People's Republic of China, Email 18157645@qq.com; Jiang Zhu, Medical Imaging Key Laboratory of Sichuan Province, North Sichuan Medical College, Nanchong, Sichuan, 637000, People's Republic of China, Email zhujiang@nsmc.edu.cn

Purpose: Phototherapy have gained significant traction in the treatment of tumors. However, the successful implementation of these therapies relies on photosensitizers with superior properties and precise guidance mechanisms.

Methods: In this study, we introduce an innovative method for the surface modification of titanium dioxide (TiO_2) nanoparticles through HRP-catalyzed covalent incorporation of Mn(II) chelate (Mn-Dopa) and dopamine.

Results: This modification extends TiO_2 nanoparticels' light absorption from ultraviolet to the near-infrared (NIR) range, endowing the nanoparticles with MRI-guided phototherapy capabilities. The resulting nanotheranostics system, TiO_2@PDA-MnDopa, demonstrated over 5-fold enhanced relaxivity compared to the monomeric MnDopa and exhibited synergistic phototherapy effects upon 808 nm laser excitation, with a photothermal conversion efficiency of 15.91%. In vitro and in vivo pharmacodynamics studies showed that the TiO_2@PDA-MnDopa demonstrated good safety in the HSC3 cell line and corresponding tumor-bearing mice, while effectively inhibiting tumor growth under 808 nm laser excitation.

Conclusion: This multifunctional nanotheranostic, integrating high relaxivity with synergistic PTT/PDT for MR imaging-guided phototherapy, holds great potential for applications in the early diagnosis, noninvasive treatment, and prognostic evaluation of oral squamous cell carcinoma.

Keywords: photodynamic therapy, photothermal therapy, oral squamous cell carcinoma, titanium dioxide, horseradish peroxidase catalysis

Introduction

Oral squamous cell carcinoma (OSCC) is a heterogeneous malignant neoplasm from oral epithelial cells and constitutes over 90% of all malignancies within the oral cavity.[1] In 2020, the global newly diagnosed OSCC cases was reported to be 377,713, with a corresponding mortality of 177,757.[2] Currently, surgical resection is the primary therapeutic intervention for OSCC, supplemented by chemotherapy and radiotherapy as the principal adjuvant.[3] However, the high recurrence rate (20–86%), and cervical lymph node (LN) metastasis often limit surgical resection as a definitive intervention treatment.[4] Concurrently, chemotherapy and radiotherapy lack of tumor specificity cause severe adverse effects on normal tissues and therapeutic resistance.[5,6] Consequently, the five-year overall survival rate remains around 60%,

Received: 1 February 2025
Accepted: 16 April 2025
Published: 12 May 2025

Graphical Abstract

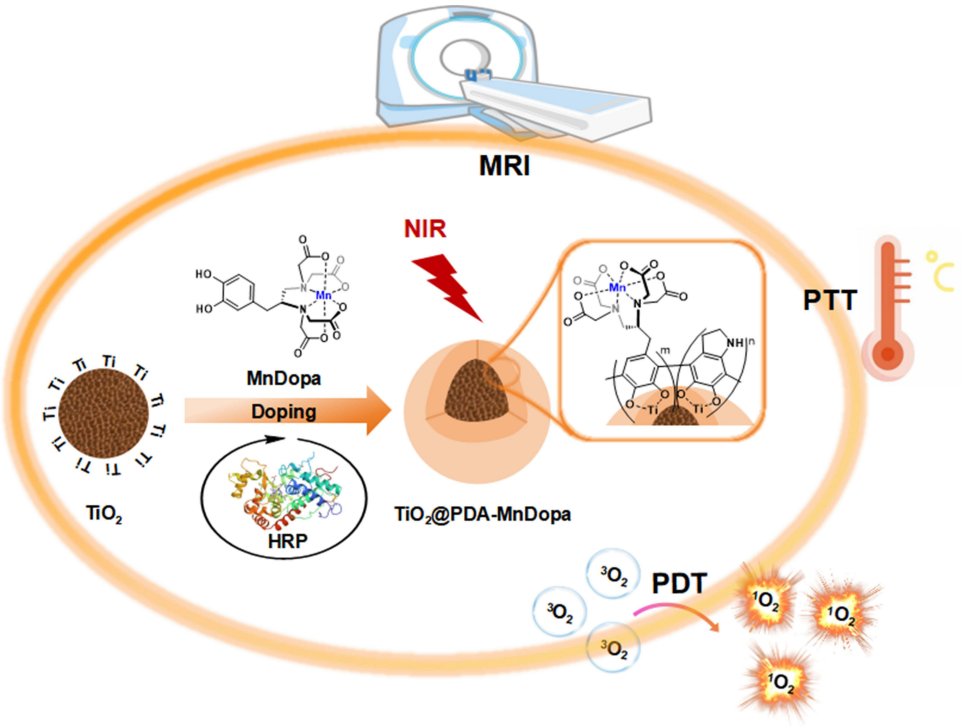

despite multimodal treatments that significantly improve quality of life.[1,7] This underscores the urgent need for more effective strategies to improve local disease control.

Phototherapy, including photodynamic therapy (PDT) and photothermal therapy (PTT), has emerged as a highly effective non-invasive therapeutic modality for the primary treatment of superficial tumors,[8] especially OSCC. These therapies utilize the spatiotemporal selectivity of photosensitizer (PS) for precise tumor targeting.[9] In PDT, PS agents generate reactive oxygen species (ROS) upon activation, inducing localized cellular damage.[10] In PTT, near-infrared (NIR) laser irradiation generates heat in situ to thermally killing cancer cells.[11] Nevertheless, the dose-dependent and unpredictable nature of ROS and heat generation can result in collateral damage to surrounding normal tissues, highlighting the urgent need for improving monitoring and control of therapeutic effects.

To address this challenge, magnetic resonance imaging (MRI) is emerging as a key auxiliary imaging modality for phototherapy and personalized nanotheranostics.[12,13] MRI offers the capability to track the real-time distribution and metabolism of nanomedicine, optimize the drug-light interval prior to irradiation, delineate tumor margins for precise targeting, evaluate therapeutic outcomes.[14] By integrating these functionality, MRI facilitates the simultaneous initiation and monitoring of intratumoral PDT and PTT, enabling the development of optimal treatment strategies with reduced side effects.

As for PSs, although traditional organic molecules had exhibited significant efficacy in generating elevated levels of ROS, they are often limited by insufficient photostability and sensitivity constraints.[15] Inorganic materials, particularly titanium dioxide (TiO_2), demonstrate long-term physical and chemical stability but are restricted by their ultraviolet light response range, which limits their applicability in deep-tissue phototherapy.[16,17] To address this challenge, polydopamine (PDA) has emerged as a multifunctional modifier. PDA not only extends TiO_2's absorption to the near-infrared (NIR) region (700–900 nm) through its strong π-conjugated electronic structure, but also synergistically enhances both PTT and PDT effects.[18–20] Specifically, PDA's abundant catechol and amine groups enable robust anchoring to TiO_2 surfaces, facilitating stable nanocomposite formation.[21,22] Moreover, PDA's redox-active quinone/catechol moieties promote electron transfer processes under NIR irradiation, which amplify TiO_2's photocatalytic activity and ROS generation

for enhanced PDT.[23,24] Concurrently, PDA's exceptional photothermal conversion efficiency (exceeding that of gold nanoparticles by over 40%) and broad NIR absorption enable efficient heat generation for PTT.[25] This dual functionality —combining TiO_2's photocatalytic behavior with PDA's photothermal and redox properties—positions the nanocomposite as an ideal platform for synergistic PTT/PDT applications.

In our previous studies, we have developed a heteroditopic Mn(II) chelate, Mn-DopaEDTA, featuring an Dopa-derived Mn-EDTA complex with a catechol group.[26] This configuration facilitates the formation of Mn-metallostar structures with high relaxivity through catechol-M (M = Fe(III) or Ti(IV)) coordination-driven self-assembly, making it highly effective as an MRI contrast agent. The Fe-Mn metallostar, in particular, demonstrates significant MRI relaxivity enhancement, over twice that of monomeric Mn-DopaEDTA, along with synergistic PTT and PDT effects when exposed to NIR light. Building on this, Mn-DopaEDTA has been utilized to coat superparamagnetic iron oxide (SPIO) nanoparticles via catechol-Fe(III) coordination on the Fe_3O_4 surface, forming SPIO@Mn-DopaEDTA structures.[27] These core-shell nanoparticles exhibit excellent water dispersibility and possesses optimized T1/T2 relaxivity properties, acting as effective dual-modal MRI contrast agents.

In this study, we develop an novel nanoplatform intergrates TiO_2 nanoparticles with PDA and Mn-DopaEDTA (MnDopa) to address the limitation of single-modality PTT or PDT. Leveraging the excellent coordination properties of catechol group, we used horseradish peroxidase (HRP) catalysis to co-deposit dopamine and Mn-Dopa onto TiO_2 surfaces, achieving surface chemical modification of TiO_2 with both Mn-Dopa and PDA.

Based on the attractive properties of high relaxivity and NIR optical absorption of the core-shell nanoparticles structure discussed above, herein we report the synthesis and characterization of a new MRI/PTT/PDT nanotheranostic TiO_2@PDA-MnDopa. To explore the performance in MRI, we studied its morphology, composition, relaxation properties and imaging effect in vivo. To evaluate the performance in PTT and PDT, we studied its photoactive characteristics, photo-therapy effect and safety in the HSC3 cell line and tumor-bearing mice. This multifunctional nanocomposite achieves synergistic PTT and PDT effects, combining PDA's photothermal properties with MnDopa's MRI imaging capability and TiO_2's photocatalytic behavior. Together, these components enable a robust, image-guided multimodel phototherapy platform with enhanced efficacy for treating oral cancer.

Materials and Methods

Materials and Apparatus

Titanium(IV) chloride, diethylene glycol (DEG), dopamine, and horseradish peroxidase (HRP) were obtained from InnoChem (Beijing, China). Additionally, 1,3-diphenylisobenzofuran (DPBF) was sourced from Macklin (Shanghai, China). The Cell Counting Kit-8 (CCK-8) and the Calcein/PI Cell Viability Assay Kit were acquired from Beyotime (Shanghai, China). Ultrapure water (Millipore Milli-Q grade, 18.2 MΩ) was utilized throughout the experiments. Manganese concentrations were measured using an inductively coupled plasma mass spectrometry (ICP-MS) system (PerkinElmer Nex-ion 350x, USA). The zeta potential was assessed using dynamic light scattering (DLS) with a Malvern Zetasizer Nano ZS90 (UK).

Balb/C male nude mice, aged 4 to 6 weeks, were procured from the Laboratory Animal Center of North Sichuan Medical College (NSMC), Sichuan, China. All experimental procedures were conducted in accordance with the Guidelines for the Care and Use of Laboratory Animals and received approval from the Ethics Committee of NSMC (Application No. 2023007).

Preparation of TiO_2@PDA-MnDopa

TiO_2 nanoparticles were synthesized following a protocol established by Bianca Geiseler et al. In summary, 0.2 mL of titanium(IV) chloride was introduced to 6 mL of diethylene glycol (DEG) while maintaining vigorous stirring under an inert atmosphere at a temperature of 60°C. A white precipitate formed immediately, after which the suspension was heated to 75°C until the solution became clear. Subsequently, 0.1 mL of double-distilled water (ddH_2O) was injected into the solution, and the mixture was refluxed at 160°C for 6 h. Upon cooling to room temperature, 15 mL of acetone was added to facilitate the precipitation of nanoparticles (NPs). The NP solution was then subjected to centrifugation at

3500 rpm for 30 min and washed multiple times with acetone to eliminate residual surfactants. The TiO_2 nanoparticles were characterized using transmission electron microscopy. The synthetic route for MnDopa was adapted from prior research.[27] TiO_2 nanoparticles (100 mg) were dissolved in 20 mL of phosphate-buffered saline (PBS) at a concentration of 50 mm and a pH of 6.5, while dopamine (71.2 mg) and MnDopa (92.2 mg) were dissolved in 5 mL of PBS under the same conditions. Dopamine and MnDopa were then gradually added to the TiO_2 solution while stirring vigorously, resulting in a color change from white to orange, indicative of the formation of a charge transfer complex. After 3 h, 1 mL of horseradish peroxidase (HRP) at a concentration of 4 mg/mL was introduced to the solution, followed by the addition of 0.5 mL of hydrogen peroxide (H_2O_2) at a concentration of 1 M every minutes. This addition caused the solution to turn brown-black rapidly. The reaction mixture was subsequently stirred overnight, and the crude product was purified using size exclusion chromatography.

Characterization of TiO_2@PDA-MnDopa

Transmission electron microscopy (TEM) and high-resolution transmission electron microscopy (HRTEM) images were acquired utilizing a Tecnai F20 transmission electron microscope. X-ray diffraction (XRD) spectra were recorded using a D8 Focus XRD diffractometer (Bruker, USA). Dynamic light scattering (DLS) measurements and Zeta potential assessments were conducted with a Nano-ZS Zeta-sizer nanosystem (Malvern, UK). X-ray photoelectron spectroscopy (XPS) analyses were performed employing an AXIS Ultra DLD XPS instrument (Kratos, UK). Fourier transform infrared (FT-IR) spectra and ultraviolet-visible (UV-vis) absorbance measurements were obtained using a Nicolet 6700 FT-IR spectrometer (Thermo Scientific, USA) and a Lambda 950 UV-vis spectrophotometer (Perkin Elmer, USA), respectively.

Relaxivity

The magnetic resonance (MR) performance was evaluated using a 0.5 T MesoMR23-060H-1 MR instrument (Niumag, China). Specifically, 1 mL of TiO_2@PDA-MnDopa at varying concentrations (Mn^{2+}: 0, 0.025, 0.05, 0.1, 0.2, and 0.4 mM) was placed in separate centrifuge tubes. T1-weighted MR imaging was subsequently conducted, and the relaxation times (T_1 and T_2) were measured. Additionally, the longitudinal (r_1) and transverse (r_2) relaxivities were calculated.

Photothermal Performance

An 808 nm laser was employed to investigate the photothermal properties of TiO_2@PDA-MnDopa, with temperature variations and corresponding images recorded using an infrared camera. (1) A range of concentrations of TiO_2@PDA-MnDopa (0, 50, 100, 150, and 200 μg/mL) were subjected to laser exposure for a duration of 10 min at a power density of 2.0 W/cm². (2) TiO_2@PDA-MnDopa at a concentration of 200 μg/mL was irradiated with the 808 nm laser at varying power densities (1.0, 1.5, 2.0, and 2.5 W/cm²) for 10 min. (3) The photostability of TiO_2@PDA-MnDopa was also assessed, wherein 1 mL of the TiO_2@PDA-MnDopa solution (200 μg/mL) was subjected to irradiation from the 808 nm laser (2.0 W/cm²) with alternating on/off cycles every 10 min for a total of five cycles.

Reactive Oxygen Species ($^1O_2$) Detection

1,3-Diphenylisobenzofuran (DPBF) was employed to quantify the singlet oxygen generated by TiO_2@PDA-MnDopa. A volume of 20 μL of DPBF (1.0 mg/mL, dissolved in DMSO) was combined with 2 mL of TiO_2@PDA-MnDopa (100 μg/mL in water) and subsequently irradiated with an 808 nm laser (1.0 W/cm²) for a duration of 10 min. The absorption spectra of DPBF were recorded and analyzed before and after irradiation. Additionally, pure DPBF and TiO_2 were subjected to irradiation with the 808 nm laser for 10 min, and the generation of reactive oxygen species (ROS) was also assessed.

Cell Cytotoxicity

HSC3 cells were obtained from the American Type Culture Collection (ATCC). The Cell Counting Kit-8 (CCK-8) assay was employed to evaluate the cytotoxicity of TiO_2@PDA-MnDopa. HSC3 cells were plated in a 96-well plate at a density of 1×10^4 cells per well and cultured for 12 h in Dulbecco's Modified Eagle Medium (DMEM) supplemented with 10% fetal bovine serum (FBS) and 1% penicillin-streptomycin solution. Following this incubation period, the medium was aspirated,

and varying concentrations of TiO_2@PDA-MnDopa (0, 25, 50, 100, 150, and 200 μg/mL) were introduced to the cells. Untreated cells, maintained in the medium alone, served as the control group. After 24 h of incubation, 10 μL of CCK-8 reagent was added to each well, and the plates were incubated for an additional 1.5 h. The absorbance of the medium containing the CCK-8 reagent was subsequently measured at 450 nm using a microplate reader.

In vitro Phototherapy

The in vitro phototherapy was assessed utilizing the CCK-8 assay. HSC3 cells were incubated with TiO_2@PDA-MnDopa at varying concentrations (0, 25, 50, 100, 150, and 200 μg/mL) for 4 h. Afterward, the medium was replaced with fresh medium, and the cells were irradiated with an 808 nm laser for 10 min at a power density of 2.0 W/cm². Following irradiation, the cells were incubated for an additional 24 h. Cell viability was then evaluated using the CCK-8 assay as previously described. Two control experiments were conducted to further investigate the relative contributions of PTT and PDT to the cytotoxicity. For PDT only: experiments were conducted as described above, but HSC3 cells were irritated with an NIR laser (808 nm, 10 min, 2.0W/cm²) at 4°C to suppress temperature elevation. For PTT only: experiments were conducted as described above, but HSC3 cells were co-incubated with a ROS scavenger (Vitamin C, 0.5 mm) to exclude the PDT effect, followed by NIR (808 nm, 10 min, 2.0W/cm²). Finally, the absorbance of each well was measured with a microplate reader at a wavelength of 450 nm.

In vitro Reactive Oxygen Species Detection

HSC-3 cells were cultured in confocal dishes at a density of 1×10^5 cells per dish for a 24-h incubation period. Subsequently, 1 mL of TiO_2@PDA-MnDopa at a concentration of 200 μg/mL was introduced, followed by an additional incubation of 4 h. After this, 1 mL of DCFH-DA at a concentration of 10 μM was added for a 20-min incubation. The dishes were then washed three times with PBS, and 1 mL of culture medium was added. Finally, the dishes were subjected to irradiation with an 808 nm laser at an intensity of 1.0 W/cm² for 5 min. The generation of reactive oxygen species (ROS) was assessed by measuring the fluorescence of 2,7-dichlorofluorescein (DCF), which is the oxidation product of DCFH-DA in the presence of ROS. This fluorescence was observed using a TSCSPS II confocal laser fluorescence microscope (Olympus, Japan), as DCF can be rapidly oxidized into a highly fluorescent green compound in ROS.

Live/Dead Staining

To visualize the HSC3 cell state, a live/dead staining experiment was conducted. HSC3 cells were evenly distributed across six confocal dishes and incubated for 24 h. Subsequently, the cells in each dish received distinct treatments: PBS as a control, laser treatment alone, TiO_2@PDA-MnDopa treatment alone, TiO_2@PDA-MnDopa at a concentration of 50 μg/mL combined with laser treatment, and TiO_2@PDA-MnDopa at a concentration of 200 μg/mL combined with laser treatment. Laser irradiation was administered after 4 h of incubation with TiO_2@PDA-MnDopa. Following an overnight incubation, a Calcein/PI Cell Viability Assay Kit was employed to co-stain the cancer cells. After 30 min, fresh DMEM medium was added to the plates in preparation for subsequent confocal imaging.

In vivo Biocompatibility with Tumor-Bearing Nude Mice Model

In the assessment of in vivo biocompatibility, healthy nude mice were administered intravenous injections of 100 μL of pure saline and TiO_2@PDA-MnDopa (20 mg/mL in saline), respectively. Following a two-week period, the mice were euthanized, and the major organs, including the heart, liver, spleen, lungs, and kidneys, were excised for analysis. Hematoxylin and eosin (H&E) staining images were subsequently examined using an optical microscope. For the HSC3 tumor-bearing nude mouse model, HSC3 cells (100 μL) suspended in DMEM medium were subcutaneously injected into the right thigh of the mice. The mice were utilized for experimentation once the tumors reached a volume of 100 mm³.

In vivo Imaging

T1-weighted magnetic resonance imaging (MRI) of HSC3 tumor-bearing nude mice was conducted using a 3.0 Tesla Discovery MR750 system (GE Medical Systems, Milwaukee, WI). An intravenous injection of 100 μL of TiO_2@PDA-

MnDopa (20 mg/mL in saline) was administered to the HSC3 tumor-bearing nude mice. Subsequently, T1-weighted MRI was performed at 0 min, 30 min, 60 min, 90 min, 120 min, and 6 h post-injection.

In vivo Anti-Tumor Therapy

Four experimental groups were established, each consisting of five mice. The mice were subjected to one of the following treatments: PBS, laser treatment alone, TiO_2@PDA-MnDopa treatment alone, or a combination of TiO_2@PDA-MnDopa and laser treatment. For the groups receiving either laser treatment alone or TiO_2@PDA-MnDopa combined with laser treatment, laser irradiation was administered 1 h post-injection of PBS (100 μL) or TiO_2@PDA-MnDopa (100 μL, 20 mg/mL) via the tail vein for 10 min. Temperature variations were monitored using a thermal camera. Three days later, a second round of laser irradiation was conducted under the same conditions. Tumor volumes and body weights of the mice were recorded every two days. After 14 days, the tumors were excised for photographic documentation and weighing.

Statistical Analysis

Data are presented as means ± SD, and statistical significance was determined using GraphPad Prism software 8. The differences between the groups were determined using using two-tailed unpaired *t*-tests. The threshold for statistical significance was set at $p < 0.05$ with 95% confidence intervals.

Results and Discussion

Synthesis and Characterization of TiO_2 and TiO_2@PDA-MnDopa

TiO_2 nanoparticles with small particle sizes were synthesized using the sol-gel method. The water solubility of these nanoparticles is attributed to the presence of diethylene glycol on their surface. The weakly bound diethylene glycol were readily replaced by the catechol groups of dopamine and MnDopa through a ligand exchange reaction. An HRP-catalyzed reaction was employed to facilitate the co-polymerization of dopamine and MnDopa, covalently incorporating them onto the TiO_2 surface to achieve stable and uniform surface modification. This innovative approach enable the precise intergration of both PDA and MnDopa onto the TiO_2 nanoparticles, forming small-sized core-shell structures with enhanced chemical stability. The resulting nanocomposites combine the photothermal properties of PDA with the MRI contrast enhancement provided by MnDopa, offering a multifunctional platform for theranostic applications.

The structural characteristics of TiO_2 were examined using high-resolution transmission electron microscopy (HR-TEM) (Figure 1A). The HR-TEM analysis revealed that TiO_2 exhibited well-defined crystalline structures. The scanning electron microscopy (SEM) image of TiO_2@PDA-MnDopa demonstrated the clustering of several nanoparticles (Figure 1B). To assess the colloidal stability of the synthesized nanoparticles, measurements of the hydrodynamic diameter and zeta potential were conducted. The average size of TiO_2 was determined to be 5.7±0.7 nm, while that of TiO_2@PDA-MnDopa was found to be 121.0±3.6 nm (Figure 1C and Table 1), indicating effective dispersion and stability due to the surface modification. Furthermore, the surface potential of TiO_2 was measured at 38.1±2.0 mV, possibly due to the existence of positively charged Ti (IV) ion on the surface of TiO_2. However, following the surface modification with PDA and MnDopa, the surface potential decreased significantly −52.4 ±1.4 mV (Figure 1D).

The elemental composition was confirmed through X-ray photoelectron spectroscopy (XPS). In the full-scan XPS spectrum, four characteristic absorption peaks related to C1s (283.75 eV, 61.22%), O1s (530.38 eV, 28.25%), N1s (398.73 eV, 5.12%), Ti2p (457.58 eV, 4.66%) and Mn2p (639.98 eV, 0.75%) were recognized (Figure 1E). In contrast, the NPs without PDA and MnDopa contained only three peaks: C1s (283.67 eV, 41.05%), O1s (528.66 eV, 41.78%), and Ti2p (457.28 eV, 16.00%). The XPS spectra of C1s, O1s and Ti2p of TiO_2 and TiO_2@PDA-MnDopa show different quantities on species, suggesting that Mn doping induces changes in the local chemical environment of C, O and Ti elements of TiO_2. Moreover, the characteristic peak of Mn2p corresponding to MnO_2 demonstrates that a considerable portion of manganese is doped into the TiO_2 (Figure 1F).

The crystal structures of TiO_2 and TiO_2@PDA-MnDopa were examined using X-ray diffraction (XRD) (Figure 1G). The XRD patterns of TiO_2@PDA-MnDopa and TiO_2 were found to be similar which indicates the presence of an amorphous structure in the PDA and MnDopa without alter the crystal structure of TiO_2. To illustrate the conjugation

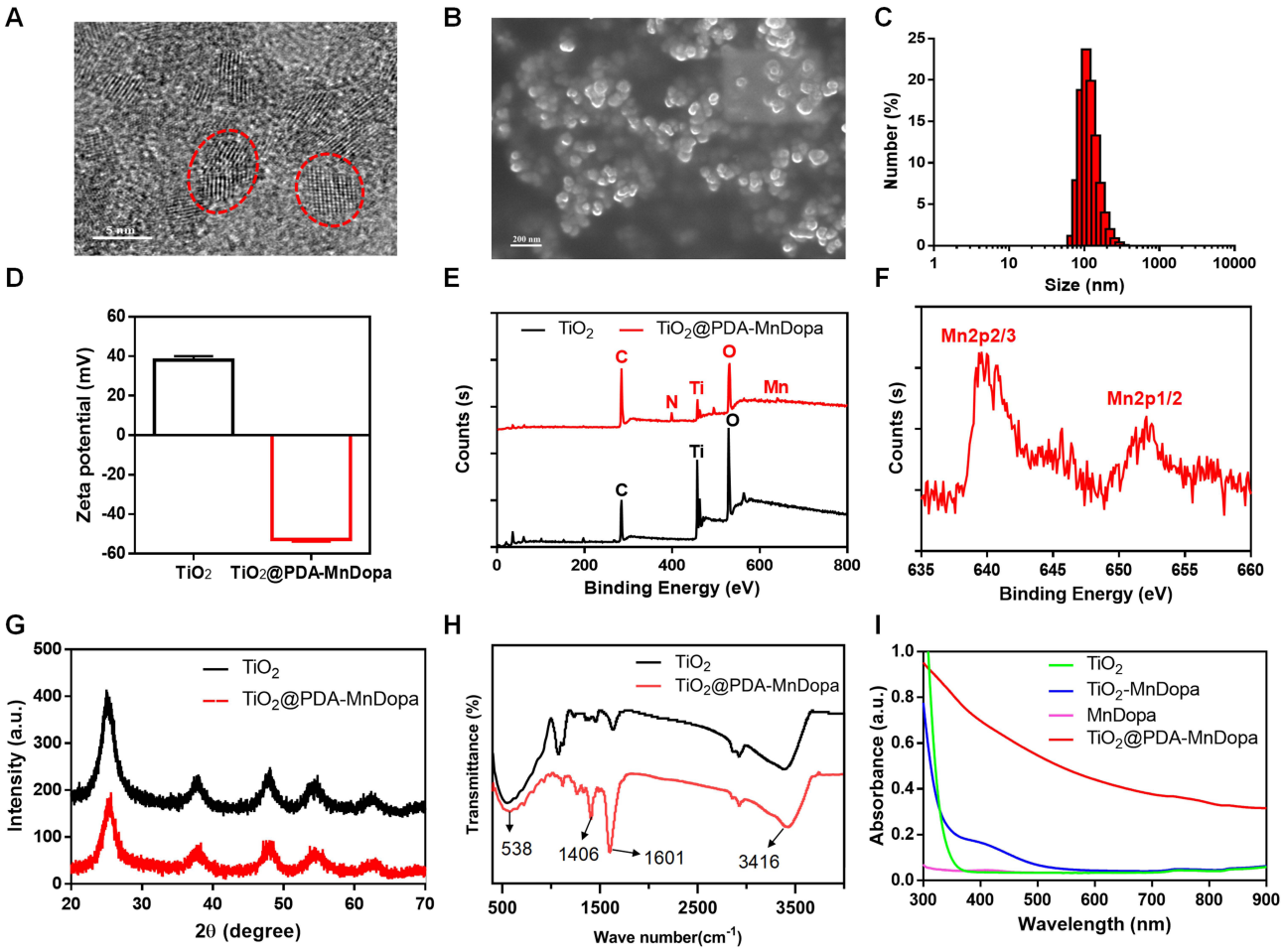

Figure 1 Physical and chemical characterization of TiO_2 and TiO_2@PDA-MnDopa. (**A**) HR-TEM of TiO_2. (Scale bar: 5 nm) (**B**) SEM of TiO_2@PDA-MnDopa. (**C**) Size of TiO_2@PDA-MnDopa. (Scale bar: 200 nm) (**D**) The zeta potentials of the TiO_2 and TiO_2@PDA-MnDopa in aqueous solution. (**E**) XPS spectra of TiO_2 and TiO_2@PDA-MnDopa. (**F**) XPS spectra of Mn 2p for the TiO_2@PDA-MnDopa. (**G**) XRD of TiO_2 and TiO_2@PDA-MnDopa. (**H**) FT-IR spectra of TiO_2 and TiO_2@PDA-MnDopa. (**I**) UV-VIS spectrum TiO_2 and TiO_2@PDA-MnDopa in aqueous solution.

process, the alterations in the surface functional groups were analyzed using Fourier Transform Infrared (FT-IR) spectroscopy. The FT-IR spectra of both TiO_2 and TiO_2@PDA-MnDopa (Figure 1H) exhibited a characteristics peak at 538 cm^{-1}, which corresponds to the Ti-O-Ti bond within the TiO_2 framework, confirming the presence of the titanium-oxygen network. Additionally, a broad absorption peaks at 3416 cm^{-1} was observed for both TiO_2 and TiO_2@PDA-MnDopa, attributed to the O-H bond stretching vibration from hydroxyl groups, which were present in both the diethylene glycol (DEG) and PDA structures. Notably, the TiO_2@PDA-MnDopa spectrum showed distinct peaks at 1406 cm^{-1} and 1601 cm^{-1}, which are assigned to the C-H bending and C=C stretching vibrations of the aromatic benzene ring in the PDA and MnDopa components, respectively. These characteristic peaks confirm the successful covalent doping of PDA and MnDopa onto TiO_2 surface.

Table 1 Physicochemical Characterization of Size, Poly Dispersibility Index (PDI) and Zeta Potential

	Size (nm)	PDI	Zeta Potential (mV)
TiO_2	5.74±0.76	0.33±0.04	38.1±1.99
TiO_2@PDA-MnDopa	121.23±3.62	0.09±0.01	−52.4±1.38

https://doi.org/10.2147/IJN.S512565

Table 2 Longitudinal (r_1) and Transverse (r_1) Relaxivity

Sample	0.5 T			1.5 T			3.0 T		
	r_1 [$mM^{-1}s^{-1}$]	r_2 [$mM^{-1}s^{-1}$]	r_2/r_1	r_1 [$mM^{-1}s^{-1}$]	r_2 [$mM^{-1}s^{-1}$]	r_2/r_1	r_1 [$mM^{-1}s^{-1}$]	r_2 [$mM^{-1}s^{-1}$]	r_2/r_1
MnDopa	3.48	4.72	1.35	3.09	6.67	2.15	–	–	–
TiO_2@PDA-MnDopa	18.17	23.97	1.31	14.76	25.99	1.76	13.05	34.56	2.64

Finally, TiO_2@PDA-MnDopa demonstrated NIR absorption in comparison to TiO_2, a feature attributed to the outer PDA shell, which is advantageous for phototherapy (Figure 1I).

Relaxation Property and Photoactive Characteristics

The longitudinal and transverse relaxivity (r_1 and r_2) of MnDopa were measured at 0.5 T as 3.48 $mM^{-1}s^{-1}$ and 4.72 $mM^{-1}s^{-1}$ (Table 2), respectively. Notably, the relaxivity of the TiO_2@PDA-MnDopa nanocomplexes was significantly enhanced, with values of r_1 = 18.17 $mM^{-1}s^{-1}$ and r_2 = 23.97 $mM^{-1}s^{-1}$, representing a 5.22-fold increase compared to the MnDopa monomer (Figure 2A). This substantial enhancement in relaxivity is attributed to the efficient intergration of MnDopa to the TiO_2 surface, which markedly slows down the rotation of MnDopa in solution. Furthermore, the TiO_2@PDA-MnDopa nanoparticles exhibited high relaxivity under higher magnetic field strengths, maintaining excellent r_1 at both 1.5 T and 3.0 T. At these field strengths, r_1 were measured at 14.76 $mM^{-1}s^{-1}$ and 13.05 $mM^{-1}s^{-1}$, respectively (Table 2). This suggests that the TiO_2@PDA-MnDopa retains high MR signal enhancement across a range of clinically relevant magnetic fields. To further validate the T1-weighted imaging (T1WI) capabilities, T1WI of aqueous TiO_2@PDA-MnDopa solutions was conducted using a 3.0 T clinical MRI scanner. The results demonstrated a significant

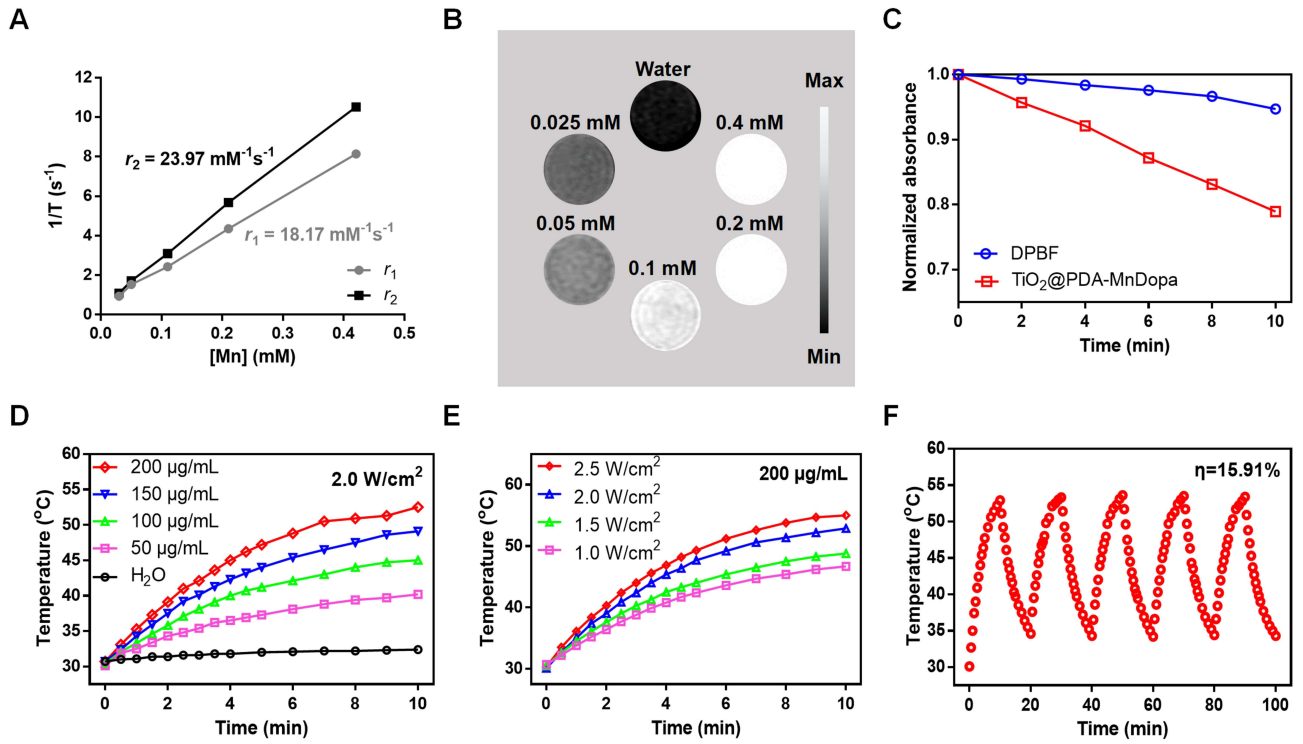

Figure 2 The Relaxation and photoactive characteristics of TiO_2 and TiO_2@PDA-MnDopa. (**A**) The longitudinal relaxation rates (r_1 and r_2) of TiO_2@PDA-MnDopa at magnetic field strengths 0.5 T. (**B**) T1-weighted imaging with different Mn(II) ion concentrations. (**C**) Generation of ROS from TiO_2 and TiO_2@PDA-MnDopa determined by a change in DPBF absorbance. (**D**) Photothermal profiles of TiO_2@PDA-MnDopa in PBS with different concentrations (50, 100, 150, and 200 μg/mL) under laser irradiation (808 nm, 2 W/cm^2). (**E**) Photothermal profiles of TiO_2@PDA-MnDopa in PBS under different power density irradiation (808 nm, 1, 1.5, 2, and 2.5 W/cm^2). (**F**) The heating curve of TiO_2@PDA-MnDopa in PBS during 5 cycles of on-and-off laser irradiation (808 nm, 2 W/cm^2).

enhancement in MR signal and increased image brightness, directly correlating with the concentration of manganese ions in the solution, thereby confirming the strong T1WI performance of the nanoparticles (Figure 2B).

To assess the photodynamic properties of TiO_2@PDA-MnDopa, the generation of ROS was monitored using 1,3-diphenylisobenzofuran (DPBF) as a singlet oxygen ($^1O_2$) scavenger. The ability of TiO_2@PDA-MnDopa to generate ROS was assessed by tracking the change in absorption at 410 nm, a characteristic peak for DPBF degradation. As illustrated in Figure 2C, following 10 min of irradiation with an 808 nm laser, there was no significant reduction in absorption for the blank control and TiO_2 samples. In contrast, the absorption of TiO_2@PDA-MnDopa decreased by 21%, indicating that TiO_2@PDA-MnDopa is capable of generating reactive oxygen species, particularly singlet oxygen, under laser irradiation.

In order to evaluate the photothermal efficacy of TiO_2@PDA-MnDopa, solutions with varying concentrations were subjected to irradiation for 10 min using an 808 nm NIR laser (2.0 W/cm²). The results indicated that the temperature of the solutions increased in response to both the irradiation time and the concentration of TiO_2@PDA-MnDopa (Figure 2D). Specifically, at a concentration of 200 μg/mL, the temperature of the solution rose from 30.7°C to 52.5°C, reflecting an increase of 21.8°C. In contrast, pure water under the same irradiation conditions experienced a temperature rise of only 1.7°C, confirming the significant PTT response of TiO_2@PDA-MnDopa.

Further experiment demonstrated that increasing the laser power enhanced the photothermal effect. At a concentration of 200 μg/mL of TiO_2@PDA-MnDopa, the solution temperature increased from 46.7°C to 55°C as the laser power was elevated from 1 W/cm² to 2.5 W/cm² (Figure 2E), demonstrating a power-dependent photothermal response.

In addition, under on-off 808 nm laser irradiation (2.0 W/cm²), the temperature of the TiO_2@PDA-MnDopa solution demonstrated consistent cycling behavior, with temperature rising and cooling processes following a predictable pattern (Figure 2F). This indicates the excellent photothermal stability of TiO_2@PDA-MnDopa.

The photothermal conversion efficiency of TiO_2@PDA-MnDopa was calculated to be approximately 15.91%, based on the temperature rise and fall curve, thereby confirming its robust photothermal conversion capability. Previous studies suggest that cancer cells are effectively eliminated at temperatures above 42°C for durations of 15–60 min, with treatment times significantly reduced (4–6s) when temperatures exceed 50°C.[28] These findings suggest that TiO_2@PDA-MnDopa has the potential to serve as an effective photothermal agent for tumor treatment.

In vitro Photo-Therapy

To investigate the capacity of TiO_2@PDA-MnDopa to generate sufficient ROS under laser irradiation, HSC3 cells were incubated with TiO_2@PDA-MnDopa and subsequently exposed to an 808 nm laser at an intensity of 1 W/cm² for 10 min. A separate group of cells treated with H_2O_2 served as a positive control, while additional groups subjected to laser irradiation alone or treated with TiO_2@PDA-MnDopa without irradiation acted as negative controls. The cells were stained with DCFH-DA, a well-established probe for ROS detection, and confocal laser scanning microscopy (CLSM) was employed to visualize intracellular ROS production. As illustrated in Figure 3A, groups exposed to either 50 mm H_2O_2 or TiO_2@PDA-MnDopa in conjunction with NIR irradiation exhibited a pronounced green fluorescence signal, indicative of ROS generation. Conversely, the negative control groups, which included cells treated solely with laser irradiation or TiO_2@PDA-MnDopa without irradiation, did not display significant detectable signals. These findings confirm that ROS can be selectively generated in cells through the uptake of TiO_2@PDA-MnDopa followed by NIR irradiation, suggesting that light-triggered TiO_2@PDA-MnDopa are promising candidates for PDT.

The phototherapy cytotoxicity of TiO_2@PDA-MnDopa on cancer cells was quantitatively assessed using a CCK-8 assay (Figure 3B). After 24 h of incubation, HSC3 cells treated with TiO_2@PDA-MnDopa without laser irradiation exhibited over 90% viability at a concentration of 200 μg/mL. In contrast, the viability of HSC3 cells decreased to less than 5% when exposed to TiO_2@PDA-MnDopa at the same concentration (200 μg/mL) and subjected to NIR laser irradiation for 10 min at a power density of 2 W/cm². To further clarify the relative contributions of photothermal and photodynamic effects to the cytotoxicity, two control experiments were performed. To investigate the photodynamic effect alone, the environmental temperature was maintained at 4°C using an ice bath to suppress hyperthermia. To study the photothermal effect alone, Vitamin C was added to scavenge singlet oxygen and shield the photodynamic effect (Figure 3B). These control experiments suggested TiO_2@PDA-MnDopa can generate synergistic photodynamic and photothermal cytotoxic effects. Notably, the photothermal effect on HSC3 cells was more potent than the photodynamic effect under the conditions tested.

https://doi.org/10.2147/IJN.S512565

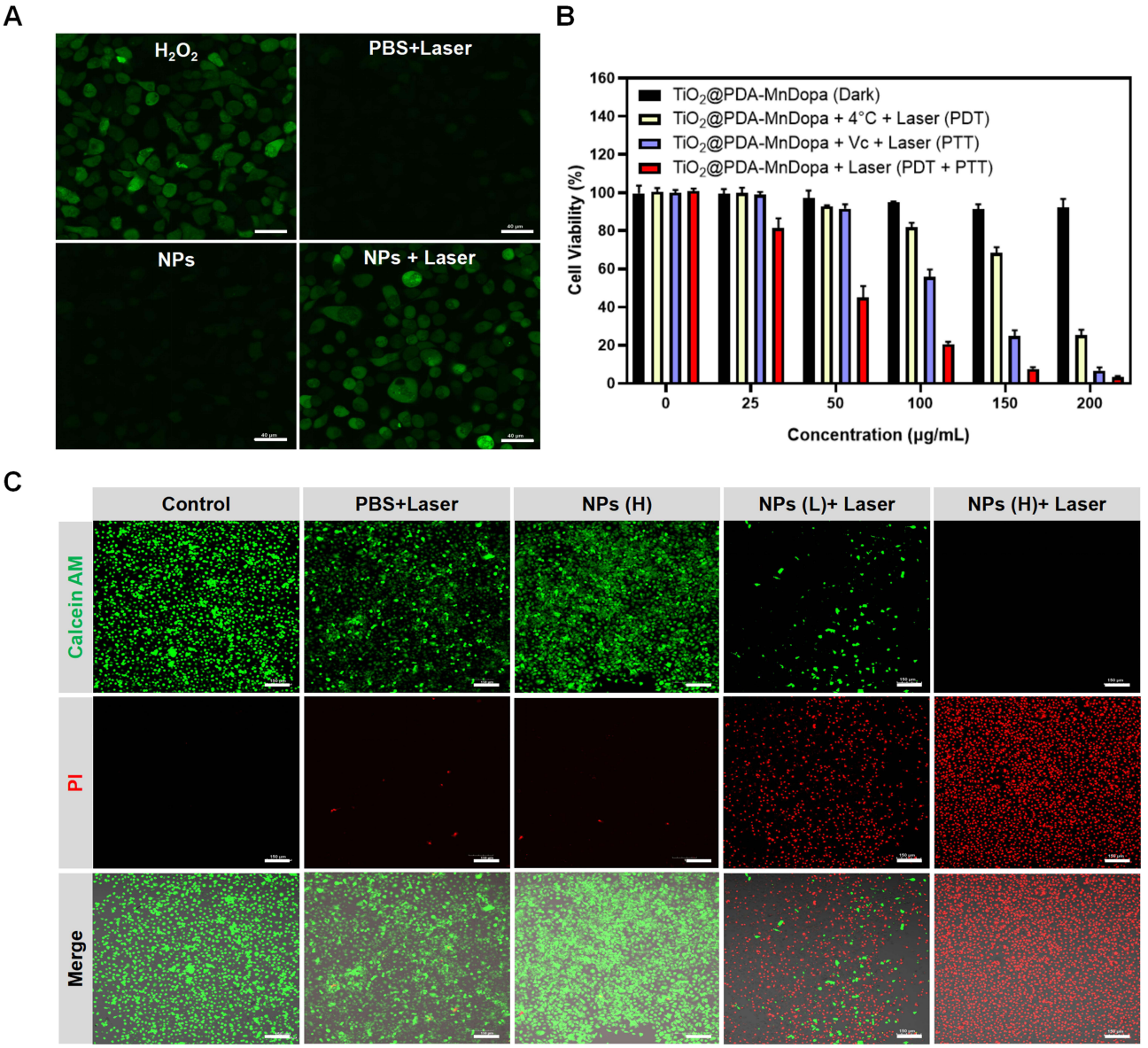

Figure 3 In vitro photo-therapy evaluation of TiO_2 and TiO_2@PDA-MnDopa. (**A**) Fluorescence microscope images of cellular ROS generation treated with TiO_2@PDA-MnDopa (50 mm). (Scale bar: 40 μm) (**B**) Relative cell viability of HSC3 cells after incubation with different concentrations of TiO_2@PDA-MnDopa for 24 h, followed by irradiation with 808 nm laser (2W/cm^2) for 10 min (4 °C was used to suppress the PTT effect and Vitamin C was used to shield the PDT effect). ***$P < 0.001$, ****$P < 0.0001$, *NS* means no significance. Data are presented as means ± SD. (**C**) Fluorescence microscope images of Calcein AM (green fluorescence, live cells) and Propidium iodide (PI, red fluorescence, dead cells) contained HSC3 cells incubated with PBS, Laser, TiO_2@PDA-MnDopa and TiO_2@PDA-MnDopa + Laser. (Scale bar: 150 μm).

Additionally, the live/dead staining experiment was conducted to visually assess the states of HSC3 cells following various treatments. As illustrated in Figure 3C, exposure to either laser or NPs alone does not affect the viability of HSC3 cells; however, the combination of NPs with laser irradiation (NPs + Laser) effectively induces cell death. An increase in the concentration of TiO_2@PDA-MnDopa, ranging from 50 to 200 μg/mL, correlates with a significant decline in the viability of HSC3 cells, which aligns with the findings from the CCK-8 assay. These results collectively indicate that TiO_2@PDA-MnDopa exhibit favorable biocompatibility in the absence of light while demonstrating efficacy in inducing cancer cell death upon exposure to 808 nm laser irradiation.

In vivo MRI-Guided Anti-Tumor Photo-Therapy

Inspired by the excellent anti-tumor effect in vitro of TiO_2@PDA-MnDopa, the efficacy of in vivo therapy was further evaluated in mice. Prior to initiating the antitumor experiment, MRI was utilized to determine the optimal time point for

laser irradiation. Following the intravenous administration of TiO_2@PDA-MnDopa (0.038 mmoL/kg), the T1-weighted MRI intensity at the tumor site exhibited a gradual increase, reaching a peaking at 1 h post-injection, and remained elevated until approximately 2 h. Notably, the signal intensity at the tumor site diminished after 6 h (Figure 4A). The normalized signal-to-noise ratio (nSNR) and the change in contrast-to-noise ratio (ΔCNR) values of the tumor tissues were quantified to assess the tumor's visibility and the quality of the MRI signal. The nSNR, which quantifies the clarity of the tumor image relative to background noise, and ΔCNR, which measures the contrast between the tumor and surrounding tissues, provide insights into the extent of TiO_2@PDA-MnDopa uptake by the tumor. Both ratios showed a significant increase after TiO_2@PDA-MnDopa injection, with peak values observed around 1 h post-injection. Specifically, the nSNR reached 1.24 ± 0.03, and ΔCNR was 10.16 ± 1.29, both showing a continued upward trend until approximately 1.5 h post-administration (Figure 4B and C). These results indicate a favorable tumor-targeting capability attributed to the enhanced permeability and retention (EPR) effect. Importantly, these findings help guide MRI-based phototherapy by providing key information on the optimal laser irradiation time and irradiation duration. The peak of the nSNR and ΔCNR indicates the ideal time point for initiating laser irradiation (around 1 h post-injection), ensuring the maximum accumulation of TiO_2@PDA-MnDopa at tumor site.

Thus, infrared thermal imaging was performed under the guidance of MRI after a 1 h post-injection, corresponding to the peak of TiO_2@PDA-MnDopa accumulation at the tumor site (Figure 4D). Following the MRI signal confirmation, the 808 nm laser was applied to the tumor region. The temperature at the tumor site in the NPs + Laser group increased by 17 °C, demonstrating effective photothermal conversion. In contrast, the temperature in the PBS+laser control group rose by only 5 °C, confirming the specific photothermal effect of TiO_2@PDA-MnDopa nanoparticles (Figure 4E).

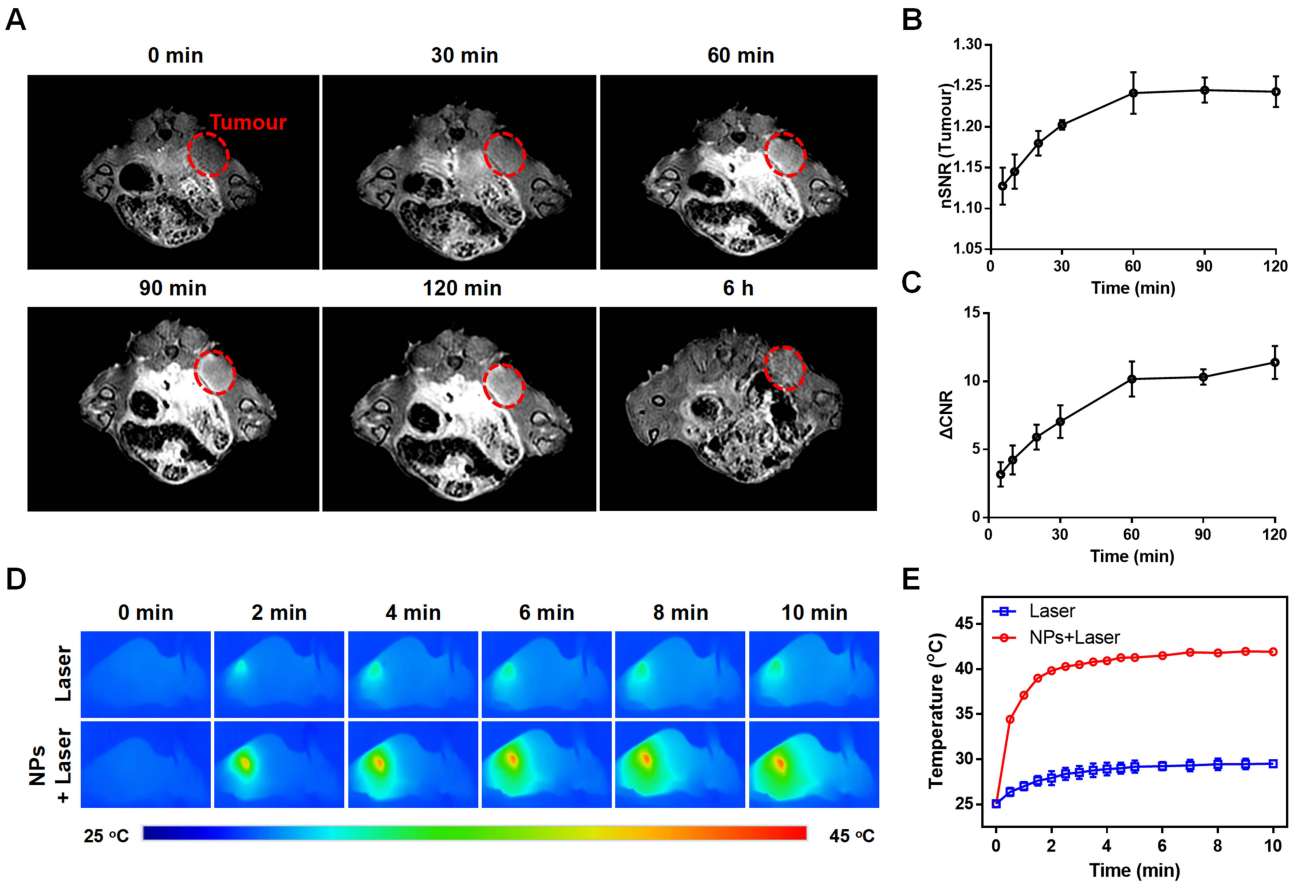

Figure 4 In vivo MRI and PTT of HSC3 tumor-bearing mice. (**A**) Representative coronal T1-weighted MR images of mice obtained prior, 30 min, 60 min, 90 min, 120 min, and 6 h after intravenous injection of TiO_2@PDA-MnDopa. (**B** and **C**) Graphs show the normalized signal-to-noise ratio (nSNR) and contrast-to-noise ratio (ΔCNR, tumour vs muscle) time course in the tumour after injection of TiO_2@PDA-MnDopa. (**D** and **E**) Photothermal images and temperature evolution of HSC3 tumor-bearing mice injected with PBS and TiO_2@PDA-MnDopa under NIR laser irradiation (808 nm, 2 W/cm^2) for 10 min at 1-h post-injection.

https://doi.org/10.2147/IJN.S512565

HSC3 tumor-bearing mice with a tumor volume of approximately 100 mm^3 were randomly divided into four groups, with five mice per group (Figure 5A). Throughout the 14-day treatment period, tumor size and body weight were monitored every two days. As shown in Figure 5B, the digital photographs taken on the 14th day post-treatment revealed complete tumor elimination in the TiO_2@PDA-MnDopa + Laser group. Tumor volumes in the control groups increased rapidly over the course of the experiment (Figure 5C–E). In comparison, the TiO_2@PDA-MnDopa and PBS+Laser

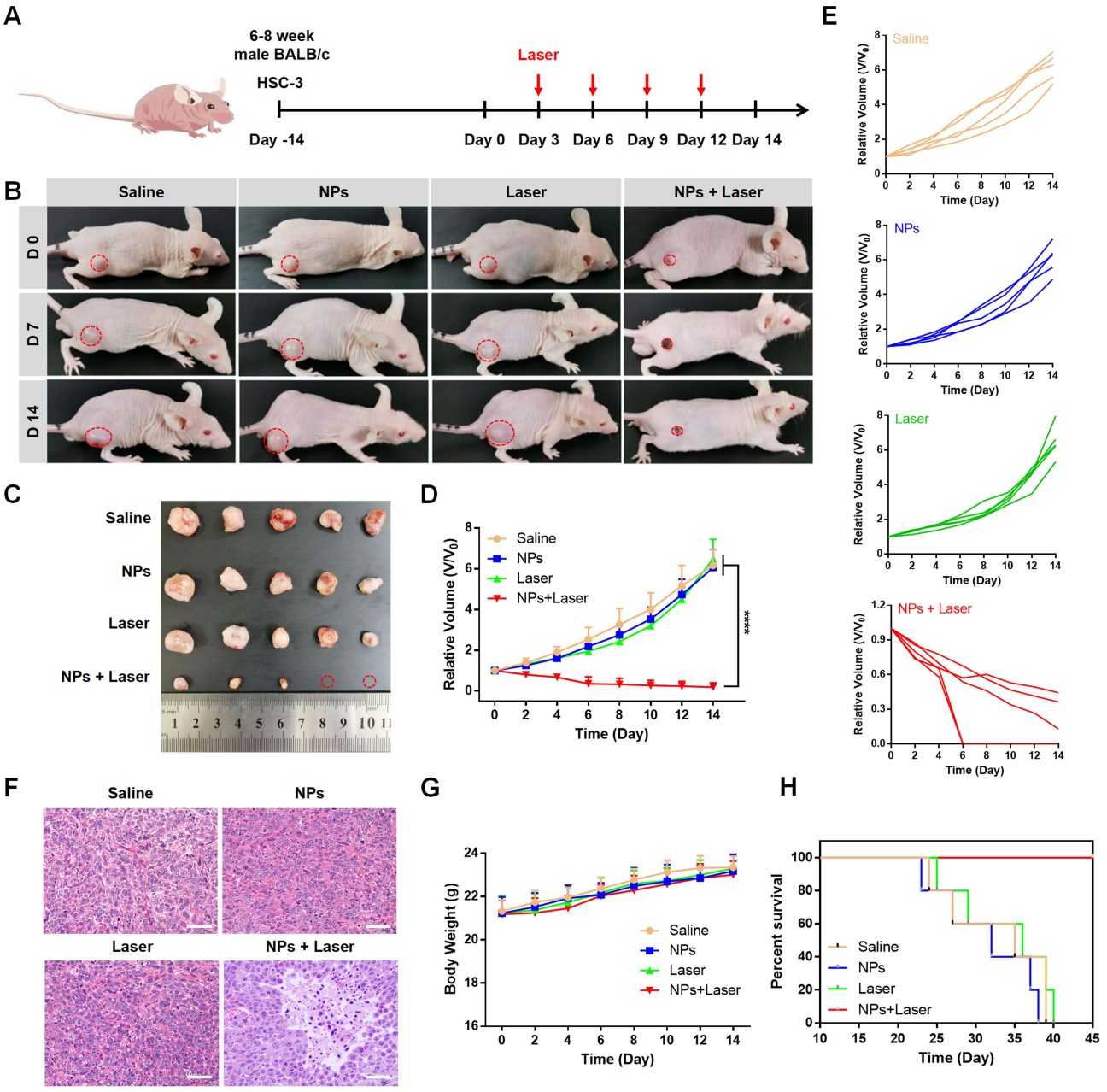

Figure 5 In vivo antitumor activity of different treatment of HSC3 tumor-bearing mice. (**A**) Scheme of HSC3 tumor-bearing mice development and photo-therapy. (**B**) Representative photos of HSC3 tumor-bearing mice after different days before (0 d) and after (7 and 14 d) different treatments. Saline, without treatment; NPs, injection of TiO_2@PDA-MnDopa only; Laser, irradiation with laser only; TiO_2@PDA-MnDopa+Laser, injection of TiO_2@PDA-MnDopa and irradiation with a laser. (**C**) Optical images of the dissected tumors from HSC3 tumor-bearing mice in different treatment groups at day 14 after sacrificing the mice. (**D** and **E**) Relative volumes of tumors after the above treatments, normalized to their initial volumes. ****$P < 0.0001$. Data are presented as means ± SD. (**F**) Histological section of tumor stained with hematoxylin and eosin after intravenous administration of TiO_2@PDA-MnDopa. (Scale bar: 50 μm) (**G**) Average body weights of mice from each group after various treatments. (**H**) Survival curves of HSC3 tumor-bearing mice in various groups after NIR-light irradiation treatment.

groups showed a slower tumor growth rate than the control groups. These results agree fairly well with the tumor growth curves, confirming the efficacy of TiO_2@PDA-MnDopa under laser irradiation.

Additionally, histological analysis using H&E staining of tumor sections showed severe cell damage in the tumors of mice from the TiO_2@PDA-MnDopa + Laser group, whereas only partial destruction of tumor cells was observed in the other treatment groups (Figure 5F). Importantly, there were no significant differences in the body weight of the mice across all groups, indicating that the treatments did not induce any overt toxicity or affect the overall health and development of the animals (Figure 5G).

The survival rate of the mice was also monitored throughout the study. After NIR laser irradiation, the TiO_2@PDA-MnDopa group exhibited the highest survival rate among all experimental groups, while the control groups showed signs of distress and succumbed after approximately 40 days (Figure 5H). These findings demonstrate the potent anti-tumor effect and safety profile of TiO_2@PDA-MnDopa-mediated phototherapy.

Conclusion

In conclusion, we have successfully synthesized a novel TiO_2@PDA-MnDopa nanocomposite that combines exceptional MRI capability with powerful PDT and PTT effects, exhibits an exceptionally strong MR signal and notable PDT and PTT capabilities. Both in vitro cellular assays and in vivo experiments demonstrated that TiO_2@PDA-MnDopa can effectively induce synergistic PDT and PTT effects upon laser irradiation. This innovative phototherapy platform, coupled with MRI guidance, shows significant potential as a multifunctional nanotheranostic agent for precise cancer diagnosis and treatment.

However, it is important to note that the animal model utilized in this study involved ectopic transplanted tumors in tumor-bearing mice, which is primarily constrained by the limitations of the imaging and treatment devices employed. Future work will focus on improving experimental equipment, refining the model to better reflect primary tumor conditions, and extending research to explore the potential of TiO_2@PDA-MnDopa for the diagnosis and treatment of primary oral cancer.

Abbreviations

TiO_2, titanium dioxide; NIR, near-infrared; OSCC, oral squamous cell carcinoma; LN, lymph node; PDT, photodynamic therapy; PTT, photothermal therapy; PS, photosensitizer; ROS, reactive oxygen species; MRI, magnetic resonance imaging; PDA, polydopamine; NPs, nanoparticles; SPIO, superparamagnetic iron oxide; MnDopa, Mn-DopaEDTA; HRP, horseradish peroxidase; DEG, diethylene glycol; DPBF, 1,3-diphenylisobenzofuran; CCK-8, Cell Counting Kit-8; ICP-MS, inductively coupled plasma mass spectrometry; DLS, dynamic light scattering; ddH_2O, double-distilled water; PBS, phosphate-buffered saline; H_2O_2, hydrogen peroxide; TEM, transmission electron microscopy; HRTEM, high-resolution transmission electron microscopy; XRD, X-ray diffraction; XPS, X-ray photoelectron spectroscopy; FT-IR, Fourier transform infrared; UV-vis, ultraviolet-visible; MR, magnetic resonance; ATCC, the American Type Culture Collection; DMEM, Dulbecco's Modified Eagle Medium; FBS, fetal bovine serum; DCF, 2,7-dichlorofluorescein; H&E, Hematoxylin and eosin.

Data Sharing Statement

The datasets used and analyzed during the current study are available from the corresponding author on reasonable request.

Ethics Approval

All experimental procedures were conducted in accordance with the Guidelines for the Care and Use of Laboratory Animals and received approval from the Ethics Committee of NSMC (Application No. 2023007).

Author Contributions

All authors made a significant contribution to the work reported, whether that is in the conception, study design, execution, acquisition of data, analysis and interpretation, or in all these areas; took part in drafting, revising or critically

reviewing the article; gave final approval of the version to be published; have agreed on the journal to which the article has been submitted; and agree to be accountable for all aspects of the work.

Funding

This work was supported by the National Natural Science Foundation of China (81671675, 21172025), the Natural Science Foundation of Sichuan Province (25NSFSC1914), the Doctoral Startup Fund of North Sichuan Medical College (Grant no. CBY24-QDA32), and the Science and Technology Project of Municipal School Strategic Cooperation, Nanchong (NSMC20170101, 18SXHZ0091, 18SXHZ0379, 20SXOT0180, 22SXQT0202).

Disclosure

The authors report no conflicts of interest in this work.

References

1. Tan Y, Wang Z, Xu M, et al. Oral squamous cell carcinomas: state of the field and emerging directions. *Int J Oral Sci*. 2023;15(1):44. doi:10.1038/s41368-023-00249-w
2. Romano A, Di Stasio D, Petruzzi M, et al. Noninvasive imaging methods to improve the diagnosis of oral carcinoma and its precursors: state of the art and proposal of a three-step diagnostic process. *Cancers*. 2021;13(12):2864. doi:10.3390/cancers13122864
3. Mohamad I, Glaun MDE, Prabhash K, et al. Current treatment strategies and risk stratification for oral carcinoma. *Am Soc Clin Oncol Educ Book*. 2023;43:e389810. doi:10.1200/EDBK_389810
4. Doll C, Mrosk F, Wuester J, et al. Pattern of cervical lymph node metastases in squamous cell carcinoma of the upper oral cavity - How to manage the neck. *Oral Oncol*. 2022;130:105898. doi:10.1016/j.oraloncology.2022.105898
5. Anand U, Dey A, Chandel AKS, et al. Cancer chemotherapy and beyond: current status, drug candidates, associated risks and progress in targeted therapeutics. *Genes Dis*. 2022;10(4):1367–1401. doi:10.1016/j.gendis.2022.02.007
6. Beckers C, Pruschy M, Vetrugno I. Tumor hypoxia and radiotherapy: a major driver of resistance even for novel radiotherapy modalities. *Semin Cancer Biol*. 2024;98:19–30. doi:10.1016/j.semcancer.2023.11.006
7. Dong L, Xue L, Cheng W, Tang J, Ran J, Li Y. Comprehensive survival analysis of oral squamous cell carcinoma patients undergoing initial radical surgery. *BMC Oral Health*. 2024;24(1):919. doi:10.1186/s12903-024-04690-z
8. Li X, Lovell JF, Yoon J, Chen X. Clinical development and potential of photothermal and photodynamic therapies for cancer. *Nat Rev Clin Oncol*. 2020;17(11):657–674. doi:10.1038/s41571-020-0410-2
9. Fan HY, Zhu ZL, Zhang WL, et al. Light stimulus responsive nanomedicine in the treatment of oral squamous cell carcinoma. *Eur J Med Chem*. 2020;199:112394. doi:10.1016/j.ejmech.2020.112394
10. Dolmans DE, Fukumura D, Jain RK. Photodynamic therapy for cancer. *Nat Rev Cancer*. 2003;3(5):380–387. doi:10.1038/nrc1071
11. Liu Y, Bhattarai P, Dai Z, Chen X. Photothermal therapy and photoacoustic imaging via nanotheranostics in fighting cancer. *Chem Soc Rev*. 2019;48(7):2053–2108. doi:10.1039/c8cs00618k
12. Cheng H, Fan X, Ye E, et al. Dual tumor microenvironment remodeling by glucose-contained radical copolymer for MRI-guided photoimmunotherapy. *Adv Mater*. 2022;34(25):e2107674. doi:10.1002/adma.202107674
13. Zheng J, Chen SH, Huang B, Zhang M, Yuan Q, Cui R. Imaging-guided precision oncotherapy mediated by nanoprobes: from seeing to curing. *Chinese Chem Lett*. 2024;35(1):108460. doi:10.1016/j.cclet.2023.108460
14. Li P, Wang D, Hu J, Yang X. The role of imaging in targeted delivery of nanomedicine for cancer therapy. *Adv Drug Deliv Rev*. 2022;189:114447. doi:10.1016/j.addr.2022.114447
15. Konopka K, Goslinski T. Photodynamic therapy in dentistry. *J Dent Res*. 2007;86(8):694–707. doi:10.1177/154405910708600803
16. Hsu CY, Mahmoud ZH, Abdullaev S, et al. Nano titanium oxide (nano-TiO2): a review of synthesis methods, properties, and applications. *Case Stud Chem Environ Eng*. 2024;9:100626. doi:10.1016/j.cscee.2024.100626
17. Ghareeb A, Fouda A, Kishk RM, El Kazzaz WM. Unlocking the potential of titanium dioxide nanoparticles: an insight into green synthesis, optimizations, characterizations, and multifunctional applications. *Microb Cell Fact*. 2024;23(1):341. doi:10.1186/s12934-024-02609-5
18. Khan H, Shah MUH. Modification strategies of TiO2 based photocatalysts for enhanced visible light activity and energy storage ability: a review. *J Environ Chem Eng*. 2023;11(6):111532. doi:10.1016/j.jece.2023.111532
19. Li J, Ke S, Yi J, et al. Surface self-modification of TiO2 for enhanced photocatalytic toluene oxidation via photothermal effect. *J Catal*. 2024;440:115846. doi:10.1016/j.jcat.2024.115846
20. Gilson RC, Black KCL, Lane DD, Achilefu S. Hybrid TiO(2)-Ruthenium nano-photosensitizer synergistically produces reactive oxygen species in both hypoxic and normoxic conditions. *Angew Chem Int Ed Engl*. 2017;56(36):10717–10720. doi:10.1002/anie.201704458
21. Huang Q, Chen J, Liu M, Huang H, Zhang X, Wei Y. Polydopamine-based functional materials and their applications in energy, environmental, and catalytic fields: state-of-the-art review. *Chem Eng J*. 2020;387:124019. doi:10.1016/j.cej.2020.124019
22. Wang Z, Xie Y, Li Y, et al. Tunable, metal-loaded polydopamine nanoparticles analyzed by magnetometry. *Chem Mater*. 2017;29(19):8195–8201. doi:10.1021/acs.chemmater.7b02262
23. Zhu M, Shi Y, Shan Y, et al. Recent developments in mesoporous polydopamine-derived nanoplatforms for cancer theranostics. *J Nanobiotechnology*. 2021;19(1):387. doi:10.1186/s12951-021-01131-9
24. Wang D, Wu H, Zhou J, et al. In Situ One-Pot Synthesis of MOF-Polydopamine Hybrid Nanogels with Enhanced Photothermal Effect for Targeted Cancer Therapy. *Adv Sci*. 2018;5(6):1800287. doi:10.1002/advs.201800287
25. Liu Y, Ai K, Liu J, Deng M, He Y, Lu L. Dopamine-melanin colloidal nanospheres: an efficient near-infrared photothermal therapeutic agent for in vivo cancer therapy. *Adv Mater*. 2013;25(9):1353–1359. doi:10.1002/adma.201204683

26. Wu H, Li Z, Liu Y, et al. Coordination-driven self-assembled Mn(II)-metallostar with high relaxivity and synergistic photothermal and photodynamic effects. *Mater Adv*. 2023;4(24):6682–6693. doi:10.1039/D3MA00762F
27. Wu C, Chen T, Deng L, et al. Mn(ii) chelate-coated superparamagnetic iron oxide nanocrystals as high-efficiency magnetic resonance imaging contrast agents. *Nanoscale Adv*. 2020;2(7):2752–2757. doi:10.1039/D0NA00117A
28. Lin LS, Cong ZX, Cao JB, et al. Multifunctional Fe_3O_4@polydopamine core-shell nanocomposites for intracellular mRNA detection and imaging-guided photothermal therapy. *ACS Nano*. 2014;8(4):3876–3883. doi:10.1021/nn500722y